



Article

# Effect of PH-Dependent Homo/Heteronuclear CAHB on Adsorption and Desorption Behaviors of Ionizable Organic Compounds on Carbonaceous Materials

Xiaoyun Li <sup>1,2,\*</sup>, Jinlong Zhang <sup>1</sup>, Yaofeng Jin <sup>1</sup>, Yifan Liu <sup>1</sup>, Nana Li <sup>1</sup>, Yue Wang <sup>1</sup>, Cong Du <sup>1</sup>, Zhijing Xue <sup>1</sup>, Nan Zhang <sup>3</sup> and Qin Chen <sup>4,\*</sup>

<sup>1</sup> Department of Environmental Science, School of Geography and Tourism, Shaanxi Normal University, Xi'an 710119, China

<sup>2</sup> International Joint Research Centre of Shaanxi Province for Pollutants Exposure and Eco-Environmental Health, Xi'an 710119, China

<sup>3</sup> Environmental Protection Department of Mahe Town, Yuyang District, Yulin 719000, China

<sup>4</sup> Northwest Land and Resource Research Center, Shaanxi Normal University, Xi'an 710119, China

\* Correspondence: lxy518@snnu.edu.cn (X.L.); chenqin@snnu.edu.cn (Q.C.)

**Abstract:** Herein, the adsorption/desorption behaviors of benzoic acid (BA) and phthalic acid (PA) on three functionalized carbon nanotubes (CNTs) at various pH were investigated, and the charge-assisted H-bond (CAHB) was verified by DFT and FTIR analyses to play a key role. The results indicated that the adsorption order of BA and PA on CNTs was different from  $K_{ow}$  of that at pH 2.0, 4.0, and 7.0 caused by the CAHB interaction. The strength of homonuclear CAHB ( $\geq 78.96$  kJ·mol<sup>-1</sup>) formed by BA/PA on oxidized CNTs is stronger than that of heteronuclear CAHB formed between BA/PA and amino-functionalized CNTs ( $\leq 51.66$  kJ·mol<sup>-1</sup>). Compared with the heteronuclear CAHB (Hysteresis index, HI  $\geq 1.47$ ), the stronger homonuclear CAHB leads to clearly desorption hysteresis (HI  $\geq 3.51$ ). Additionally, the contribution of homonuclear CAHB ( $\geq 52.70\%$ ) was also greater than that of heteronuclear CAHB ( $\leq 45.79\%$ ) at pH 7.0. These conclusions were further confirmed by FTIR and DFT calculation, and the crucial evidence of CAHB formation in FTIR was found. The highlight of this work is the identification of the importance and difference of pH-dependent homonuclear/heteronuclear CAHB on the adsorption and desorption behaviors of ionizable organic compounds on carbonaceous materials, which can provide a deeper understanding for the removal of ionizable organic compounds by designed carbonaceous materials.

**Keywords:** ionizable organic chemicals; hydrogen bond; desorption hysteresis; carbonaceous materials; density functional theory

**Citation:** Li, X.; Zhang, J.; Jin, Y.; Liu, Y.; Wang, Y.; Du, C.; Xue, Z.; Zhang, N.; Chen, Q. Effect of PH-Dependent Homo/Heteronuclear CAHB on Adsorption and Desorption Behaviors of Ionizable Organic Compounds on Carbonaceous Materials. *Int. J. Environ. Res. Public Health* **2022**, *19*, 12118. <https://doi.org/10.3390/ijerph1912118>

Academic Editor: Fei Wang

Received: 24 August 2022

Accepted: 22 September 2022

Published: 25 September 2022

**Publisher's Note:** MDPI stays neutral with regard to jurisdictional claims in published maps and institutional affiliations.



**Copyright:** © 2022 by the authors. Licensee MDPI, Basel, Switzerland. This article is an open access article distributed under the terms and conditions of the Creative Commons Attribution (CC BY) license (<https://creativecommons.org/licenses/by/4.0/>).

## 1. Introduction

Ionizable organic compounds (IOCs), such as antibiotics, pesticides, endocrine disrupting compounds, perfluoroalkyl substances, and many personal care products, are produced on a large scale and widely used in industry, agriculture and everyday life [1,2]. Therefore, release of IOCs into the environment is inevitable, and many of them are widely detected in industrial effluents, surface and ground waters [3–5]. Due to their relatively high hydrophilicity, it is easy for IOCs to migrate and transform in the natural environment [1,6,7], thus causing potential toxic effects on aquatic organisms and human health through the food chain [8,9]. Therefore, it is very necessary and urgent to better understand the fate of IOCs, and further to effectively remove IOCs from the aquatic environment [1,10,11].

Adsorption as a highly efficient and environmentally friendly method of pollutant removal has been widely used in the removal of IOCs in water [12,13]. It is very common

for multiple pH-dependent IOC species to coexist in the same environmental system, and pH would play a vital key in regulating the proportion of their existing forms [14,15]. Thus, the adsorption behavior of IOCs could vary significantly across a broad scale depending on a wide pH range of natural water bodies from 2.2–9.8 [8,16,17]. Numerous studies have shown that the adsorption mechanisms of IOCs on carbonaceous materials mainly include hydrophobic,  $\pi$ – $\pi$  electron donor–acceptor ( $\pi$ – $\pi$  EDA), electrostatic and hydrogen bond (H-bond) interactions, and different mechanisms may act simultaneously [18–20]. As for H-bond, previous studies mainly focused on ordinary H-bond [21–23], namely weak electrostatic interactions caused by permanent and instantaneous dipoles of molecules. Recently, Ni et al. [24] first proposed a negative charge assisted hydrogen bonding (CAHB) between aromatic carboxylate ions and biochar, and then the CAHB adsorption mechanism has been gradually verified and widely assumed in subsequent studies between IOCs and functionalized adsorbents [25–29]. CAHB is much stronger and more stable than ordinary H-bond, and its strength increases with decreasing  $|\Delta pK_a|$  ( $<5.0$ ) between the hydrogen donor and acceptor [30,31]. This CAHB adsorption theory provides a new perspective for further understanding the environmental behavior of IOCs. However, to date, most of the studies on CAHB adsorption mechanism have only focused on the observation of apparent phenomena (such as the rising of the solution pH) [24], thermodynamic theoretical analysis [26,32], and density functional theory (DFT) calculation [29]. Additionally, the calculation of DFT only considered O—H $\cdots$ O (homonuclear H-bond), while there is a lack of discussion on N—H $\cdots$ O/O—H $\cdots$ N (heteronuclear H-bond). In addition, the spectral evidence for homonuclear and heteronuclear CAHB formation at the molecular scale still needs further probing.

The existing species of IOCs are mainly dependent on the solution pH. When  $pH < pK_a - 2$  or  $pH > pK_a + 2$ , only one IOC species is dominant in the solution. Thus, the adsorption behavior of the IOCs is controlled by the dominated IOC species. However, when at intermediate pH, two or more than two types of IOC species co-exist in the same system, and the whole adsorption of IOCs becomes a combined performance of different species. Up to the present, it is still a challenge to accurately calculate the adsorption contributions of different IOC species at a pH nearby the  $pK_a$  of IOCs [14]. In addition, except for pH and  $\Delta pK_a$  values between the donor and acceptor, homonuclear (O—H $\cdots$ O) or heteronuclear H-bond (N—H $\cdots$ O/O—H $\cdots$ N) may also affect the adsorption affinity of IOCs on adsorbents, thereby influencing their environmental behavior. In order to comprehend the adsorption mechanism and environmental behavior of IOCs even better, three different types of functionalized multiwalled carbon nanotubes (CNTs) were selected as the representative material in the present study to explore the effects of pH,  $\Delta pK_a$ , and homonuclear/heteronuclear H-bond properties on CAHB formation between IOCs and carbonaceous materials.

Benzoic acid (BA) and phthalic acid (PA), because of their similar molecular structure and different  $pK_a$  values, are chosen as representatives for IOCs. BA is commonly used as food additives or flavoring agents in pharmaceutical and cosmetic products [33]. PA is also an important organic industrial product, and its derivatives are widely used in plasticizers, synthesis dyes, polyester resins, polyester fibers, medicines, and personal care products [34]. BA and PA have both been frequently detected in groundwater, surface water, and surface soil [35–38]. Previous studies pointed out that both BA and PA would have adverse effects on human health and the water environment [33,39–41].

The aims of this study are (1) to illustrate the dominant adsorption mechanism of BA and PA on different functionalized CNTs under various pHs; (2) to obtain spectral evidence for homonuclear and heteronuclear CAHBs formation between BA/PA and CNTs; (3) to explore the effect of homonuclear/heteronuclear CAHB and solution pH on adsorption behaviors of IOCs by CNTs; (4) to further clarify the adsorption mechanism and configuration of different CAHBs by DFT calculation. This study will further deepen our understanding of the role and influence of CAHB in the environmental behavior of IOCs and provide new directions for the management of IOCs in wastewater.

## 2. Materials and Methods

### 2.1. Adsorbents, Chemicals, and Characterization

Three types of zigzag multi-walled CNTs, including oxygen-rich (O-CNTs), amino-rich (N-CNTs), and graphitized carbon nanotubes (G-CNTs), were obtained from Chengdu Organic Chemicals Co. Ltd., Chinese Academy of Sciences. All used CNTs were characterized for their surface morphologies with TEM (JEM-2100, Japan) and SEM (FEI Quanta 200, USA). The total elemental composition and the surface elemental composition were analyzed by an elemental analyzer (Vario ELIII, Germany) and XPS (AXIS-ULTRA, Japan), respectively. A full-automatic surface area and pore distribution analyzer (ASAP2460, Micromeritics, USA) was used for the surface area determination at 77 K, and surface functional groups were examined by FTIR (Tensor 27, Bruker, Germany) at 298.15 K with the range of 4000–400  $\text{cm}^{-1}$ . The  $\xi$ -potential was determined with a Nano Zeta Sizer (Bi-90 plus, Brookhaven, USA), and the buffering capability was also determined independently by titration with 0.2 g CNTs (pH from 2.0 to 12.0). All the characterization processes and results were displayed in Text S1 and Table S1, respectively. BA and PA (purity  $\geq 99\%$ ) were bought from Sigma-Aldrich and utilized without any other process. Selected properties of adsorbates were presented in Table S2. Other chemicals and reagents used in the experiment, such as  $\text{NaN}_3$ , HCl, NaOH, NaCl, and acetonitrile, were all guaranteed reagents. All experiments utilized Milli-Q water.

### 2.2. Batch Adsorption and Desorption Experiments at Different pHs

The batch equilibrium adsorption assays of BA and PA on three types of CNTs were carried out in 8 mL glass vials. 200  $\text{mg}\cdot\text{L}^{-1}$   $\text{NaN}_3$  (biocides) and 0.02  $\text{mol}\cdot\text{L}^{-1}$  NaCl were added to ultra-pure water to prepare the background solution, and then the solutions of BA or PA at different concentrations (0–150  $\text{mg}\cdot\text{L}^{-1}$ ) were generated in the background solution, and the pH was adjusted to 2.0, 4.0, or 7.0 using HCl or NaOH. An amount of 50 mg CNTs was first pre-wetted in 1 mL of background solution with the same pH for 48 h in a glass vial as the desired concentration of BA/PA solution. Following that, 7 mL of the required adsorbate solution was added, and the mixed vials were shaken for another 48 h (no significant difference after 48 h, Figure S1) in the dark ( $25 \pm 1$  °C) at 180 rpm. After centrifugation (3000 rpm for 30 min), the supernatant firstly passed through the micropore membrane filter (0.45  $\mu\text{m}$ ) and then the concentration of adsorbates was determined via HPLC (Thermo U3000, USA) with a C18 column at 226 nm and 231 nm for BA and PA, respectively. All adsorption tests were conducted at least twice.

Desorption tests were only performed at pH 2.0 and 7.0. After reaching the adsorption equilibrium (48 h), 4 mL of the supernatant was removed and then 4 mL of background solution with the same pH was added. The vials were sealed and continued to shake for an additional 48 h (Figure S1), and then sampled in accordance with the instructions provided in adsorption tests. The supernatant concentration of BA/PA was measured by HPLC. The desorption number of IOCs was computed according to the concentration difference before and after desorption. All desorption assays were carried out with two parallels.

Adsorption kinetics of BA and PA on O-CNTs at pH 7.0 was investigated by using batch equilibration technique and all the experiments were performed with at least two replications. A previous study indicated that the effect of equilibrium time on the initial environmental factors was negligible [42]. Therefore, the initial concentration of BA or PA was 50  $\text{mg}\cdot\text{L}^{-1}$  to determine adsorption kinetics. The contact time was set to 1 h, 5 h, 10 h, 24 h, 48 h, and 72 h, respectively. Each sample was centrifuged, filtered, and determined by HPLC immediately after taking it out.

### 2.3. Data Analysis

The adsorption kinetic data were fitted employing the pseudo-first-order, pseudo-second-order, and intra-particle diffusion models, and the isothermal adsorption data

were fitted by the Freundlich and Langmuir models. The optimal fitting model was considered using lower sum of squares residual (SSR) values and higher adjusted square of correlation coefficient (Adj  $r^2$ ) values. The adsorption affinity of IOC<sub>s</sub> on CNT<sub>s</sub> could be described through the distribution coefficient ( $K_d$ ). All of the above-mentioned formulas and analysis procedures were fully described in Text S2.

The desorption extent was reflected by release ratio ( $R_r$ ) [43] and hysteresis index (HI) [44]:

$$R_r (\% \text{ of adsorbed}) = \frac{Q_e - Q_{\text{desorption3}}}{Q_e} \times 100\% \quad (1)$$

$$\text{Hysteresis index (HI)} = \frac{Q_e^d - Q_e^s}{Q_e^s} \Big|_{T, C_e} \quad (2)$$

where  $Q_e$  ( $\text{mg} \cdot \text{g}^{-1}$ ) and  $Q_{\text{desorption3}}$  ( $\text{mg} \cdot \text{g}^{-1}$ ) are the equilibrium adsorption concentration and the equilibrium adsorption concentration after the third desorption step.  $Q_e^d$  ( $\text{mg} \cdot \text{g}^{-1}$ ) is solid-phase solute concentration at desorption equilibrium, and  $Q_e^s$  ( $\text{mg} \cdot \text{g}^{-1}$ ) is the solid-phase solute concentration derived from the liquid-phase solute concentration  $C_e$  ( $\text{mg} \cdot \text{L}^{-1}$ ) depending on the assumption that adsorption is totally reversible. The closer HI is to 0, the lower degree of desorption hysteresis is. The subscripts T and  $C_e$  denote the temperature and solute equilibrium concentration respectively.

#### 2.4. DFT Computational Details

DFT calculation was carried out to better discern the homonuclear/heteronuclear CAHB interaction between adsorbates and CNT<sub>s</sub>. The B3LYP functional and the 6-311 + G\*\* basis set were used in the Gaussian 09W software package for energy computation and geometric optimization, and the DFT-D3(BJ) dispersion correction was performed [29]. The polarizable continuum model (PCM) implicit solvent model (water) was employed to account for solvation effects. The model of G-CNT<sub>s</sub> that is typically employed is the armchair CNT<sub>s</sub> (3, 3) with 48 C atoms [45,46]. Moreover, the number of functional groups on the tips is usually more than that on the sidewalls of CNT<sub>s</sub> because of the highest defect sites on the tips [47,48]. Hence, O-CNT<sub>s</sub> and N-CNT<sub>s</sub> were simulated by attaching functional groups of  $-\text{OH}/-\text{COOH}$  and  $-\text{NH}_2$  to the tips of the G-CNT<sub>s</sub>. The optimized structures of neutral O-CNT<sub>s</sub>, N-CNT<sub>s</sub>, and IOC<sub>s</sub> are shown in Figure S2. The binding energy ( $E_{\text{ads}}$ ) of homonuclear/heteronuclear CAHB formed between IOC<sub>s</sub> and O-CNT<sub>s</sub>/N-CNT<sub>s</sub> was calculated via Eq. (3) [46,49]:

$$E_{\text{ads}} = E_{(\text{CNTs} + \text{IOC})} - E_{\text{CNTs}} - E_{\text{IOC}} \quad (3)$$

where  $E_{\text{CNTs} + \text{IOC}}$  represents the total energy of IOC<sub>s</sub> on CNT<sub>s</sub>,  $E_{\text{CNTs}}$  is the total energy of CNT<sub>s</sub>,  $E_{\text{IOC}}$  is the total energy of IOC<sub>s</sub>. The obtained  $E_{\text{ads}}$  was also corrected by equilibrium correction method considering the basis set superposition error (BSSE).

### 3. Results and Discussion

#### 3.1. Characterization of CNTs

The TEM (A, B, and C) and SEM (D, E, and F) images of three CNT<sub>s</sub> are presented in Figure S3. It can be found that the surface roughness of O-CNT<sub>s</sub> and N-CNT<sub>s</sub> was more obvious than that of G-CNT<sub>s</sub>, and CNT<sub>s</sub> tubes were obviously bent or broken due to structural defects after oxidized or ammoniated modification, thereby leading to their specific surface area increase in the order (Table S1) of G-CNT<sub>s</sub> ( $66.87 \text{ m}^2 \cdot \text{g}^{-1}$ ) < O-CNT<sub>s</sub> ( $81.50 \text{ m}^2 \cdot \text{g}^{-1}$ ) < N-CNT<sub>s</sub> ( $172.61 \text{ m}^2 \cdot \text{g}^{-1}$ ). In addition, the longer chain of amine provided larger pore volume is also an important reason for the significantly larger specific surface area of N-CNT<sub>s</sub>, especially the pore volume within the range of 9–76 nm (Figure S4). The presence of the different functional groups on the CNT<sub>s</sub> surface causes a change in the  $\text{pH}_{\text{PZC}}$  of the adsorbents [42]. The  $\text{pH}_{\text{PZC}}$  of O-CNT<sub>s</sub> and N-CNT<sub>s</sub> are 3.07 and 8.76, respectively (Figure 1A). The lack of functional groups on the G-CNT<sub>s</sub> surface is likely responsible for

its unstable PZC. The titration results of the buffering capability of different CNTs are shown in Figure 1B. The  $\text{pH}_{\text{PZC}}$  of the tested CNTs was determined by taking the intersection of the lines  $\text{pH}(\text{final}) = \text{pH}(\text{initial})$ , which is similar to those of the zeta potential discussed above. Compared to the G-CNTs (6.60), the decline in the  $\text{pH}_{\text{PZC}}$  of the O-CNTs (3.65–4.22) is mainly because of the introduction of the acidic O-groups on the surface. However, the introduction of amino groups on the CNTs surface results in an increase in  $\text{pH}_{\text{PZC}}$  of N-CNTs (8.46–8.67).

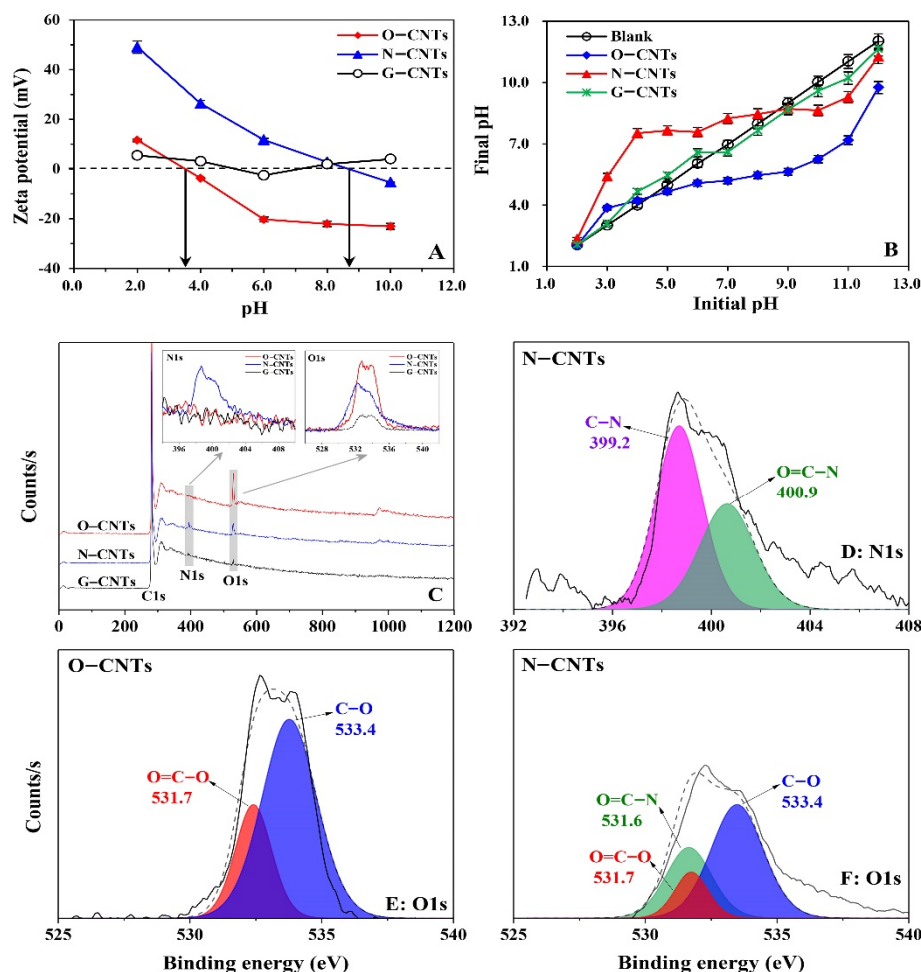


**Figure 1.** (A): Zeta potential of the adsorbents in aqueous solution. The data points in the graph were averaged using three parallel sets. (B): Titration curves of the three adsorbents. Blank is background solution only with the same amount of HCl/NaOH as to the samples. (C): XPS spectra and high-resolution spectra (O1s and N1s) for O-CNTs, N-CNTs, G-CNTs (survey scans the spectral region from 0 to 1200 eV). Peaks fitting for N1s (D: N-CNTs) and O1s (E: O-CNTs, F: N-CNTs).

The peaks fitting of O 1s spectra (Figures 1E,F and S5) display that peaks at 531.6, 531.7, and 533.4 eV correspond to O=C-N, O=C-O, and C-O, respectively [18,43]. The two peaks at 399.2 eV and 400.9 eV are ascribed to the groups of C-N and O=C-N [44], respectively, which showed up in the peaks fitting of N 1s spectra (Figure 1D). To further gain more information about the surface functional groups on CNTs, FTIR spectra of the three CNTs are recorded and depicted in Figure S6. The strong peaks at 3465 and 1640  $\text{cm}^{-1}$  in O-CNTs and N-CNTs can be assigned to the stretching vibration of the O-H and C=O groups. The weak peaks at 3465 and 1640  $\text{cm}^{-1}$  also appear in G-CNTs, which is consistent with the above XPS result. In addition, the FTIR spectra of N-CNTs show two bands at 3433 and 1570  $\text{cm}^{-1}$ , corresponding to the in-plane bending mode of the primary amine  $\text{NH}_2$  and the bending mode of the secondary amine N-H, respectively, further demonstrating the existence of the amide functional groups on N-CNTs surface. The band at 3160

$\text{cm}^{-1}$  is considered the red-shift peak of  $\text{NH}_2$ , which is attributed to the overlapping bands of the  $\text{NH}_2$  and  $\text{O-H}$  [45]. A broad band between  $616\sim 810\text{ cm}^{-1}$  is caused by the out-of-plane  $\text{NH}_2$  bending mode [46]. Another important new adsorption band is the stretching of the  $\text{C-N}$  bond present in N-CNTs at  $1142\text{ cm}^{-1}$ , which further indicates the successful formation of the saturated primary amine on the CNTs surface.

### 3.2. Adsorption Kinetics of BA and PA on CNTs

Adsorption kinetics and adsorption equilibrium time of BA and PA on O-CNTs at pH 7.0 were evaluated (Figure 2 Panel I). The adsorption capacities of both BA and PA go up with increasing contact time, and 48 h is sufficient for adsorption equilibrium of BA and PA on O-CNTs to be achieved. There are three distinct stages to the adsorption process. In the first stage, the adsorption amount ( $Q_t$ ) increased rapidly within the initial 10 h owing to the adequate adsorption sites on the surface of O-CNTs for removal of BA and PA. Then, in the second stage within the 10–24 h, it proceeded at an obviously slower rate and finally reached saturation at 48 h.

The adsorption kinetics results fitting by the pseudo-first-order and pseudo-second-order models are shown in Figure 2A and Table S3. According to the bigger correlation coefficient  $\text{Adj } r^2$  (0.9998 for BA and 0.9997 for PA) and the smaller SSR (0.758 for BA and 0.953 for PA), and the closer values between the experimental adsorption capacity  $Q_{e,\text{exp}}$  (BA:  $2.29\text{ mg}\cdot\text{g}^{-1}$ , PA:  $2.96\text{ mg}\cdot\text{g}^{-1}$ ) and the maximum capacity  $Q_{e,\text{cal}}$  calculated by the pseudo-second-order model (BA:  $2.34\text{ mg}\cdot\text{g}^{-1}$ , PA:  $3.00\text{ mg}\cdot\text{g}^{-1}$ ), the pseudo-second-order model is found to be more accurate for comprehending the adsorption kinetic data of both BA and PA on O-CNTs. These results imply that the adsorption rate was mainly controlled by chemical processes performed on the O-containing functional group sites of the O-CNT surface [47]. In other words, the chemical adsorbent-adsorbate interaction is predominantly responsible for the adsorption of BA and PA on O-CNTs at pH 7.0. Notably, the adsorption rate ( $k_2$ ) of PA ( $70.95\text{ g}\cdot\text{mg}^{-1}\cdot\text{h}^{-1}$ ) on O-CNTs was more than 8 times higher than that of BA ( $8.71\text{ g}\cdot\text{mg}^{-1}\cdot\text{h}^{-1}$ ) on O-CNTs, which may be due to the fact that  $\Delta\text{pK}_a$  between PA and O-CNTs is less than 3.0, thus two  $\text{COOH}$  ( $\text{pK}_{a1}=2.98$ ,  $\text{pK}_{a2}=5.28$ , Table S2) on PA could both generate a strong CAHB interaction with O- groups on O-CNTs surface ( $\text{PZC}\approx 3.07$ , Table S1), leading to a remarkable augment in the adsorption rate.

To identify the main rate-controlling step, the intra-particle diffusion model was further employed to analyze the kinetic data of BA and PA on O-CNTs. According to Figure 2B, the linear plots of  $Q_t$  vs.  $t^{0.5}$  not only did not cross the origin and appeared to be multi-linear, but also had very poor linear regression coefficients ( $\text{Adj } r^2$ : 0.7376 for BA and 0.4622 for PA, Table S3), which indicates that this model was not applicable, and there must be an additional rate-controlling step in addition to intra-particle diffusion. [47,48]. It may be concluded that during the adsorption process, both intra-particle diffusion and external surface adsorption were active simultaneously. In addition, the values of  $C$  (the intercept of the  $Q_t$  vs.  $t^{0.5}$  plots) can provide some useful information. The external surface adsorption becomes more prominent as the rate-limiting step when the value of  $C$  is higher [47]. Regarding the values of  $C$  ( $1.38\text{ mg}\cdot\text{g}^{-1}$  for BA and  $2.26\text{ mg}\cdot\text{g}^{-1}$  for PA) in this study, the external surface diffusion has a greater impact on the adsorption rate of PA on O-CNTs than that of BA on O-CNTs, which is consistent with the above conclusion that both  $\text{COOH}$  of PA could involve in a strong CAHB surface interaction with O-groups of O-CNTs.

### 3.3. Adsorption Isotherms of BA and PA on CNTs-effect of pH

In this study, isothermal adsorption experiments were performed under pH 2.0, 4.0, and 7.0. In order to more accurately evaluate the impacts of various surface functional groups (e.g.,  $-\text{OH}$ ,  $-\text{COOH}$ ,  $-\text{NH}_2$ ) on the CNTs adsorbing BA and PA, all equilibrium adsorbed concentrations ( $Q_e$ ) were normalized to a specific surface area. The equilibrium adsorption data were analyzed by the Freundlich and Langmuir models (Figure 2 Panel II and Table S4), respectively. In terms of the greater  $\text{Adj } r^2$  ( $\geq 0.9488$ ) and lower SSR ( $\leq$

0.0177) values of the Freundlich model than that of the Langmuir model ( $\text{Adj } r^2 \geq 0.8696$ ,  $\text{SSR} \leq 0.0581$ ), and some abnormal  $Q_0$  values of the Langmuir model, the Freundlich model is selected to fit the data of BA and PA on different CNTs at various pHs.

As seen from Figure 2 Panel II, adsorption of BA and PA on various CNTs after normalization to a specific surface area at different pH conditions revealed different trends. At pH 2.0, both BA (> 99%,  $pK_a = 4.17$ , Figure S7) and PA (> 92%,  $pK_{a1} = 2.98$ ,  $pK_{a2} = 5.28$ ) predominantly existed as molecules. Their relatively large hydrophobicity ( $\text{Log}K_{ow} = 1.63$  for BA and  $\text{Log}K_{ow} = 1.24$  for PA, Table S2) at pH 2.0 resulted in the highest adsorption capacity of BA and PA on G-CNTs. For BA, the higher adsorption amount on O-CNTs per unit surface area than that on N-CNTs may be due to the repulsion (between N-CNTs and  $\text{BA} \cdots \text{H}_3\text{O}^+$ ) caused by the greater electro-positivity of N-CNTs ( $\text{PZC} \approx 8.76$ , Figure 1). For PA, about 8% of them existed as  $\text{PA}^{-1}$ , which could interact with O-CNTs and N-CNTs by electrostatic attraction and H-bond except for the hydrophobic effect. When the solution pH increased to 4.0, about 48% of BA was converted to  $\text{BA}^{-1}$ . Due to the decrease in hydrophobicity caused by this transformation, the adsorption amount of BA on O-CNTs should also be reduced. In fact, the adsorption amount of BA on O-CNTs per unit surface area not only did not decrease, but also obviously increased instead. According to our previous research, this is mainly because the strong homonuclear CAHBs [ $\text{CNTs-O}^- \cdots \text{H}^+ \cdots \text{OOC-BA}$  or  $\text{CNTs-COO}^- \cdots \text{H}^+ \cdots \text{OOC-BA}$ ] were formed between BA-1 and O-CNTs due to their small  $|\Delta pK_a| = |\text{PZC}_{\text{O-CNTs}} - pK_{a,\text{BA}}| \approx 0.52$  [18]. However, the adsorption of BA on N-CNTs was markedly reduced. Although in theory, the weak heteronuclear CAHBs [ $\text{CNTs-NH}_2 \cdots \text{H}^+ \cdots \text{OOC-BA}$ ] can also be formed between N-CNTs and BA, the contribution of this interaction is very limited due to the large  $|\Delta pK_a| = |\text{PZC}_{\text{N-CNTs}} - pK_{a,\text{BA}}| \approx 4.59$  between BA and N-CNTs. While for PA, about 88% of PA existed in  $\text{PA}^{-1}$  forms at pH 4.0. An interesting observation is that the adsorption of PA on N-CNTs per unit surface area did not decrease as significantly as that of BA, which should be caused by the electrostatic attraction and the heteronuclear CAHBs formed between PA and N-CNTs due to their relatively smaller  $|\Delta pK_a| = |\text{PZC}_{\text{N-CNTs}} - pK_{a,\text{PA}}| \approx 3.48$ . At pH 7.0, > 99% of BA and > 96% of PA existed in the form of  $\text{BA}^{-1}$  and  $\text{PA}^{2-}$ , respectively, and the surface of O-CNTs was negatively charged as well, while N-CNTs were positively charged. In theory, the adsorption of both BA and PA on O-CNTs should be the lowest because of electrostatic repulsion between them, while their adsorption on N-CNTs should be the highest on account of electrostatic attraction. However, the fact is that the adsorption amount of both BA and PA on O-CNTs was the highest (Figure 2G,H), which indicates that the smaller  $\Delta pK_a$  between BA/PA and O-CNTs makes the strength of the homonuclear CAHB much stronger than that of the heteronuclear CAHB between BA/PA and N-CNTs.

To further explore the adsorption mechanism of BA and PA on CNTs at different pHs, the change in distribution coefficient ( $K_d$ ) was employed to understand the key role of CAHB in the adsorption process. A previous study has shown that the  $K_d$  could accurately understand the adsorption capacity of pollutants on carbon nanomaterials [11]. As shown in Figure 2 Panel III, the trends of  $\text{Log}K_d$  for BA and PA on O-CNTs and N-CNTs are different at various pHs. For O-CNTs, with the pH increase from 2.0 to 4.0, the  $\text{Log}K_{ow}$  of BA and PA clearly decreased (Table S2), but the  $\text{Log}K_d$  values of BA and PA on O-CNTs almost did not change. Obviously, the unreduced  $\text{Log}K_d$  at pH 4.0 compared to pH 2.0 is attributable to the formation of strong homonuclear CAHBs between  $\text{BA}^{-1}/\text{PA}^{-1}$  (Figure S7) and O-containing functional groups of O-CNTs. This strong CAHB interaction could counteract the effect of hydrophobicity reduction. However, for N-CNTs, the  $\text{Log}K_d$  values of BA on N-CNTs decreased sharply with the increase in pH from 2.0 to 4.0. On the one hand, the contribution of CAHB between BA and N-CNTs was limited due to the larger  $\Delta pK_a \approx 4.59$ . On the other hand, due to the formation of heteronuclear CAHB between BA and N-CNTs, the weak adsorption energy of heteronuclear CAHB could not offset the effect of hydrophobicity reduction (see Section 3.5 for detailed discussion). Interestingly, the  $\text{Log}K_d$  values of PA on N-CNTs did not decrease significantly with the increase in pH from 2.0 to 4.0. This is due to the smaller  $\Delta pK_a \approx 3.48$  between PA and N-



CNTs, which could form a relatively strong heteronuclear CAHB. Notably, at pH 7.0, the  $\text{Log}K_d$  values of BA and PA on both O-CNTs and N-CNTs are the lowest due to the extremely low hydrophobicity of BA and PA ( $\text{Log}K_{ow} = -1.20$  for BA and  $\text{Log}K_{ow} = -3.65$  for PA, Table S2). However, at pH 7.0, more than 99%  $\text{BA}^{-1}$  and more than 96%  $\text{PA}^{-2}$  could form homonuclear/heteronuclear CAHB with the functional groups on the surface of O-CNTs and N-CNTs. This strong CAHB interaction may lead to irreversible adsorption, and the specific analysis would be discussed in the next section.

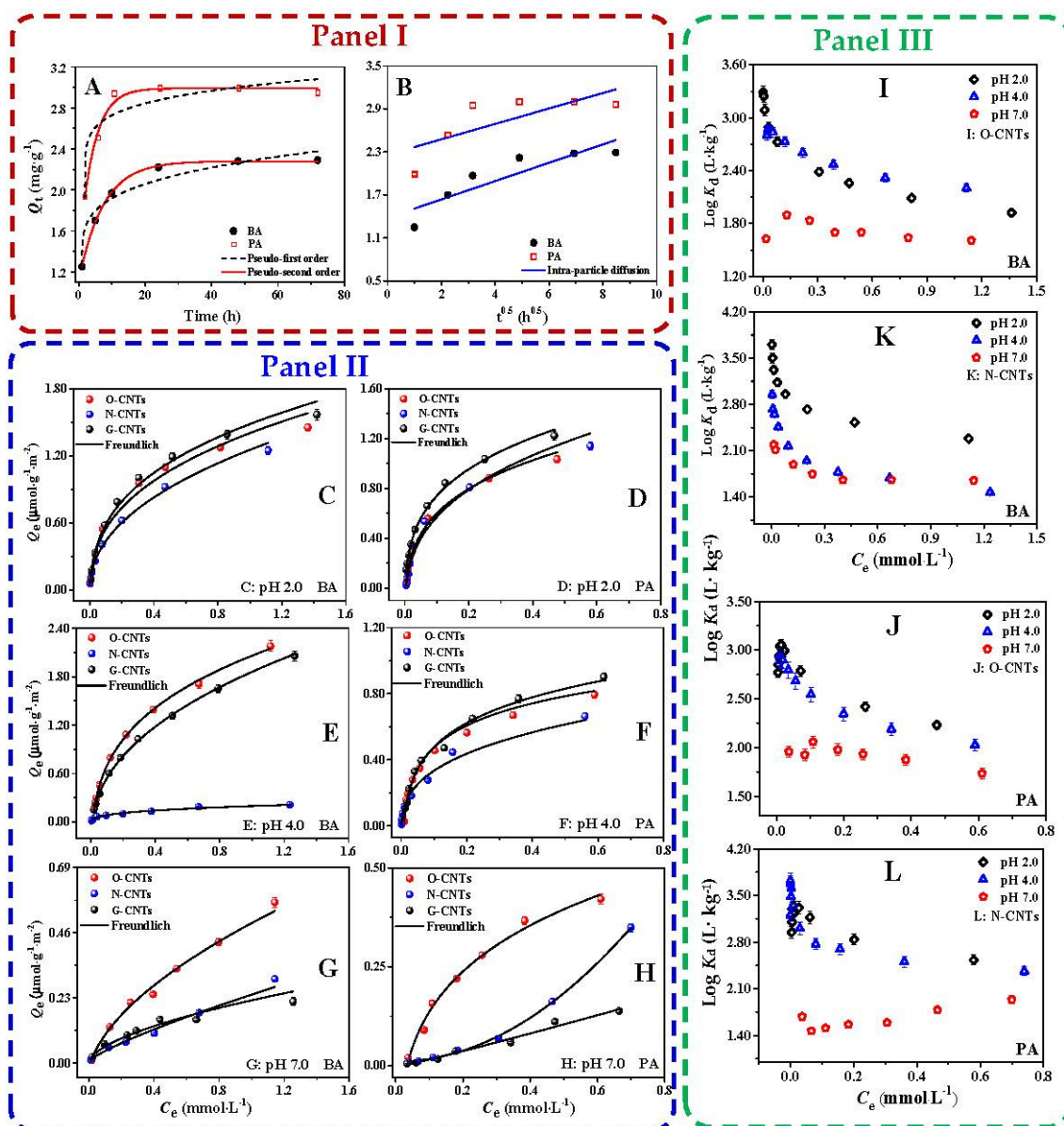


**Figure 2.** Panel I: The fitting results for (A) pseudo-first order, pseudo-second order and (B) intra-particle diffusion kinetic models of BA and PA on O-CNTs.  $C_{\text{initial}} = 50 \text{ mg} \cdot \text{L}^{-1}$ , pH = 7.0,  $T = 25^\circ \text{C}$ ,  $m/V = 0.625 \text{ g} \cdot \text{L}^{-1}$ , contact time = 72 h. Panel II: Adsorption isotherms of BA (C,E,G) and PA (D,F,H) on CNTs at different pHs after surface area normalization. Panel III:  $\text{Log}K_d$  values of BA (I,K) and PA (J,L) on O-CNTs and N-CNTs with increasing equilibrium concentration at different pH conditions. Error bars may be covered by symbol.



### 3.4. Desorption of BA and PA on CNTs at Different pHs

At pH 2.0, 99% BA and 92% PA are molecular states, while at pH 7.0, 99% BA and 96% PA exist in anion form (Figure S7). The main adsorption mechanism of BA/PA on CNTs was significantly different due to their different existence forms at different pHs. In order to investigate the difference in main adsorption mechanisms between BA/PA in molecular and anionic forms on CNTs, three adsorption–desorption cycles were carried out at pH 2.0 and pH 7.0 to further explore the contribution of CAHB to the adsorption of BA (Figure 3) and PA (Figure S8) by CNTs. The degree of irreversible adsorption was expressed by the hysteresis index (HI, Table S5). The smaller the HI values, the lower degree of desorption hysteresis [49]. At pH 2.0, because BA and PA mainly existed in molecular states, ordinary H-bond,  $\pi$ – $\pi$ , and hydrophobic interactions should be the main adsorption mechanisms, while CAHB had little contribution to the adsorption process. Thus, there is no obvious desorption hysteresis on all three CNTs at various concentrations ( $HI \leq 0.23$ , Figures 3 and S8, Table S5). However, at pH 7.0, except for G-CNTs, BA<sup>−</sup> and PA<sup>2−</sup> showed apparent desorption hysteresis of varying degrees on both O-CNTs ( $HI \geq 3.51$ , Figures 3G and S8G, Table S5) and N-CNTs ( $HI \geq 1.47$ , Figures 3H and S8H, Table S5). It may be because ionic state of BA and PA at pH 7.0 could form homonuclear/heteronuclear CAHB on O-CNTs and N-CNTs, resulting in irreversible adsorption. However, for G-CNTs, the insignificant hysteresis ( $HI \leq 0.99$ , Figures 3I and S8I, Table S5) may be attributed to the limited contribution of CAHB due to a trace group on its surface. These results are consistent with the discussion in the above section and well confirm the important role of CAHB in the adsorption of IOCs on functionalized CNTs.

Moreover, the contribution of CAHB in the process of adsorption and desorption was quantitatively calculated by release ratio ( $R_r$ ) (Table S5). At pH 2.0, the main adsorption mechanisms of BA/PA on all three CNTs were ordinary H-bond,  $\pi$ – $\pi$ , and hydrophobic interactions. Therefore, the fluctuation range of  $R_r$  values was not large (35.53% ~ 56.69%). However, at pH 7.0, the  $R_r$  values of BA/PA on all three CNTs fluctuated greatly (1.75% ~ 59.27%), which could be explained by the CAHB adsorption theory. On the one hand, the anion state of BA/PA could form homonuclear/heteronuclear CAHB with O-CNTs and N-CNTs, resulting in lower  $R_r$  values ( $\leq 17.51\%$ ). On the other hand, the main adsorption mechanisms of BA/PA on G-CNTs were  $\pi$ – $\pi$  and hydrophobic interactions because of the lack of functional groups on G-CNTs, resulting in the increase in  $R_r$  values to 59.27%. Meanwhile, it was found that the contribution of homonuclear CAHB (BA: 54.17% and PA: 52.70%) was greater than that of heteronuclear CAHB (BA: 42.55% and PA: 45.79%) at pH 7.0 (Table S5). This may be because the  $\Delta pK_a$  absolute values between BA (0.52)/PA (0.67) and O-CNTs were smaller than that between BA (4.59)/PA (3.48) and N-CNTs (Table S1 and S2), leading to the greater intensity of homonuclear CAHB than that of heteronuclear CAHB. Hence, the different contributions were determined by the strength of CAHB, which would be further discussed in the next section. These results show that different species of IOCs lead to different mechanisms under the regulation of pH, which is very important to control the pollution tendency of IOCs.

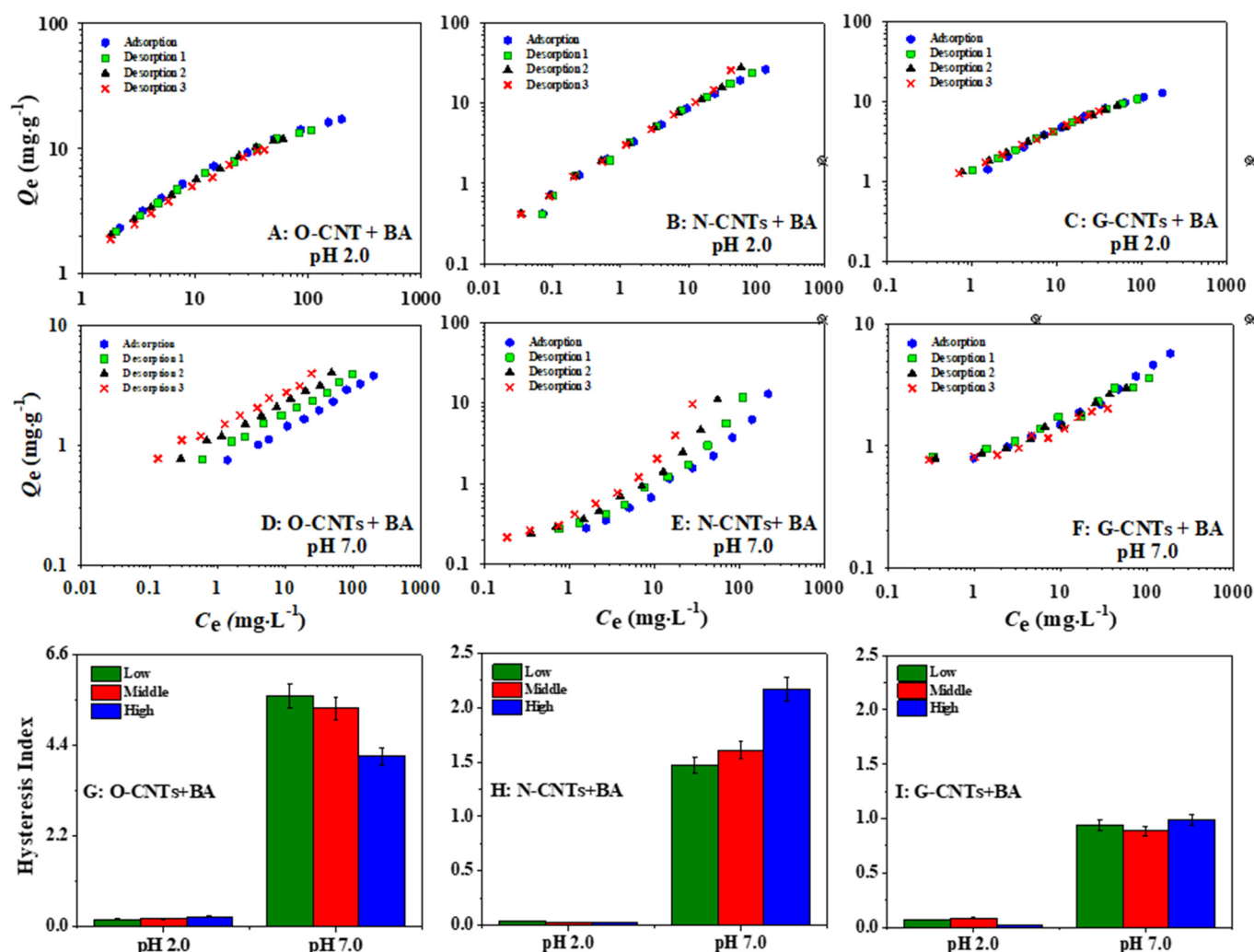


**Figure 3.** Adsorption and desorption of BA on O-CNTs, N-CNTs and G-CNTs at pH 2.0 (A–C) and pH 7.0 (D–F), respectively. And the comparison of the hysteresis index of BA (Low, Middle and High represent 5 mg·L<sup>−1</sup>, 80 mg·L<sup>−1</sup> and 160 mg·L<sup>−1</sup> of BA) on three types of CNTs (G–I) at pH 2.0 and pH 7.0. At Ph 2.0, there is no obvious desorption hysteresis of BA on three CNTs, but the obvious desorption hysteresis of BA on O-CNTs and N-CNTs occurred at pH 7.0. The hysteresis index of BA on O-CNTs ( $\geq 4.12$ ) and N-CNTs ( $\geq 1.47$ ) is higher than that of BA on G-CNTs ( $\leq 0.99$ ) at pH 7.0.

### 3.5. XPS, FTIR, and DFT Analysis of Homonuclear/Heteronuclear CAHB

In order to explore the spectral evidence of homonuclear/heteronuclear CAHB in molecular structure and compare the strength of homonuclear/heteronuclear CAHB, XPS, FTIR, and DFT analyses were further performed to verify the above adsorption mechanism. The XPS spectra of three CNTs with loaded and unloaded IOCs at pH 2.0 and 7.0 were compared and the results showed in Figure 4. It can be clearly seen from Figure 4A–D that, after adsorption of BA or PA at both pH 2.0 and 7.0, the contents of O and N functional groups on the O-CNTs and N-CNTs surface were both significant decreases, which can be attributed to these surface O and N functional groups involved into the hydrogen bond interactions between BA/PA and O-CNTs/N-CNTs. Conversely, the content of O groups on the G-CNTs surface was increased. This is mainly because the lack of functional groups on the surface of G-CNTs led to BA/PA adsorption on the surface of G-CNTs mainly through  $\pi$ – $\pi$  and hydrophobic interactions. Therefore, the O groups of BA/PA were exposed on the surface, resulting in the increase in O content of G-CNTs with loaded BA/PA.

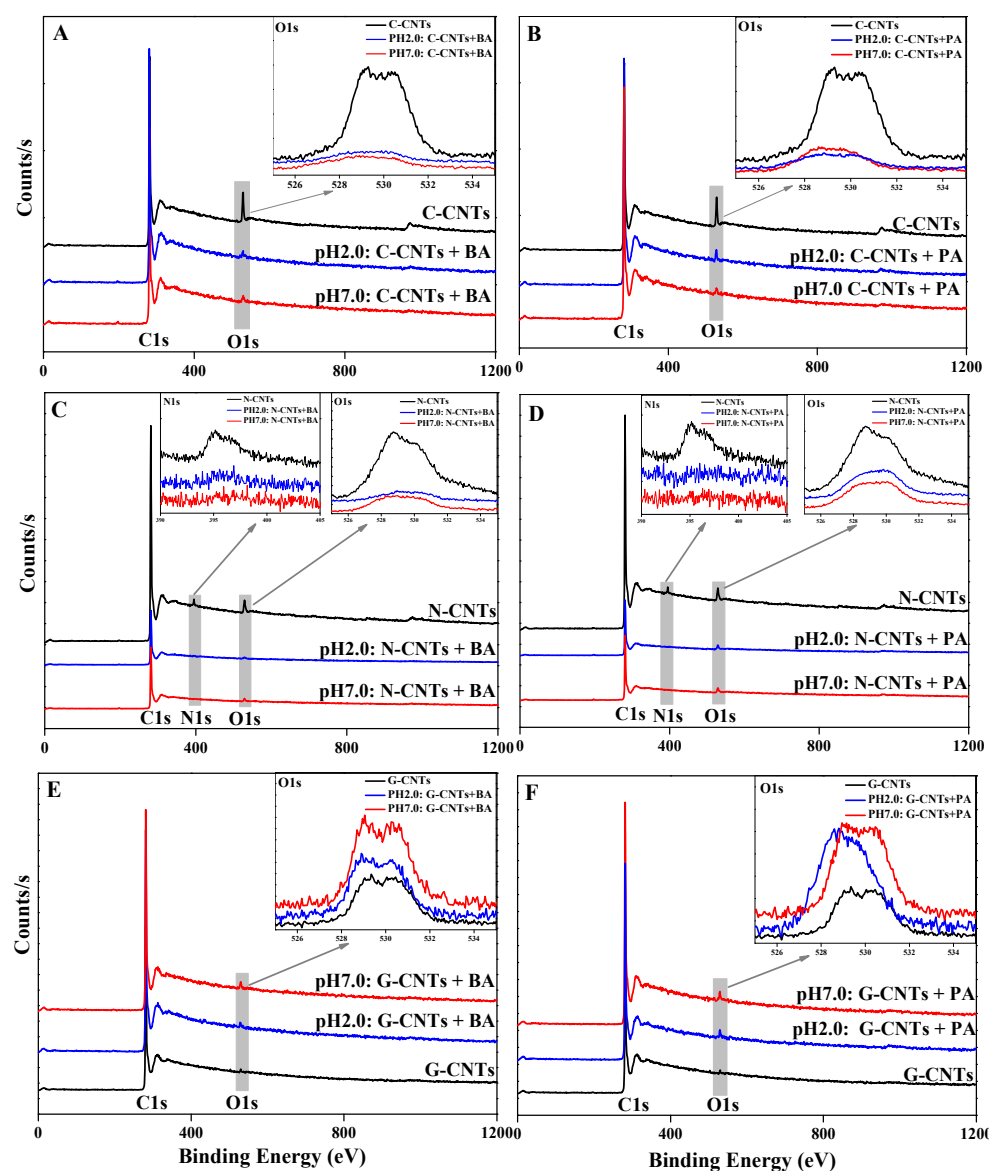


**Figure 4.** The XPS spectra of O-CNTs (A,B), N-CNTs (C,D), and G-CNTs (E,F) with loaded and unloaded IOC.

Previous studies indicated that the blue shift of the characteristic peaks in FTIR (moving to higher frequencies) revealed the special strong H-bond with rising intensity and curtate distance between the donor and acceptor [50,51], which was confirmed in our previous work [18]. As shown in Figure 5A, two obvious characteristic peaks for O-CNTs before adsorption were observed attributed to  $3465\text{ cm}^{-1}$  (O-H) and  $1640\text{ cm}^{-1}$  (C=O), respectively. After BA or PA adsorption, although the intensity of the above two characteristic peaks on O-CNTs slightly decreased at pH 2.0, the position of the absorption peaks did not change. This result indicates that BA and PA could interact with the O-H and C=O functional groups on O-CNTs surface by ordinary H-bond. However, at pH 7.0, these two peaks ( $3465\text{ cm}^{-1}$  and  $1640\text{ cm}^{-1}$ ) have undergone obvious changes or even lost after O-CNTs adsorbing BA or PA. Meanwhile, a new peak with a higher frequency ( $3660\text{ cm}^{-1}$ ) emerged, which could be attributed to the strong homonuclear CAHB formation between BA/PA and O-CNTs, resulting in the blue shift of the -OH peak.

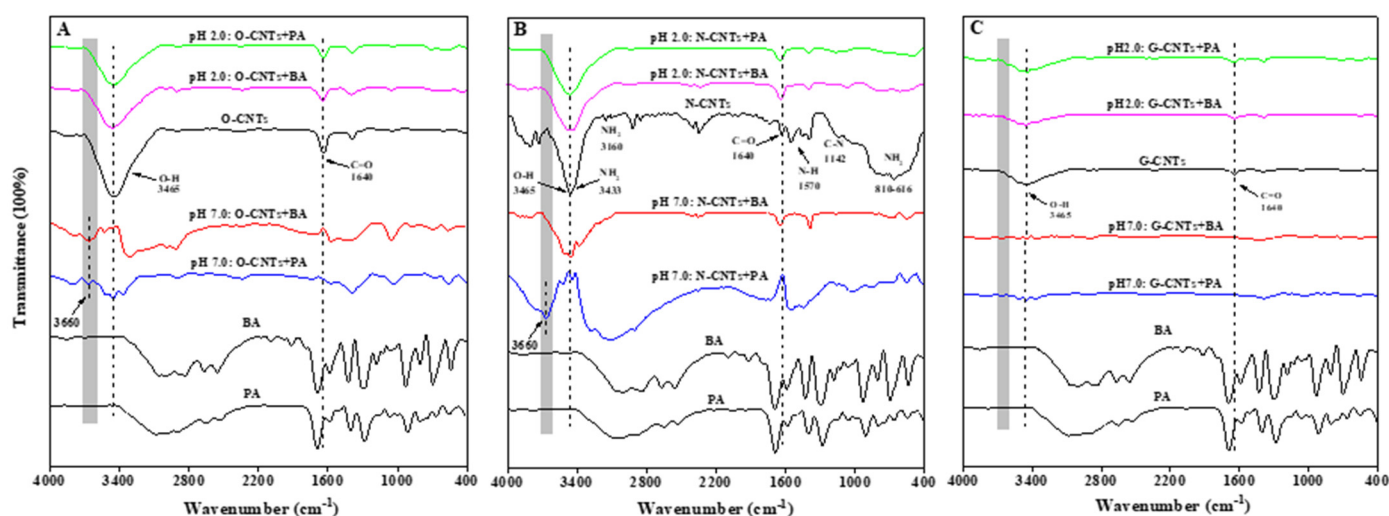


**Figure 5.** FTIR spectra analysis of before and after adsorption of BA and PA on the O-CNTs (A), N-CNTs (B) and G-CNTs (C) at pH 2.0 and 7.0, respectively. A clearly new peak appeared at the higher frequency (3660  $\text{cm}^{-1}$ , the blue shift of O-H or  $-\text{NH}_2$ ) reveals the formation of the homonuclear CAHB or heteronuclear CAHB.

For N-CNTs (Figure 5B), after adsorption of BA or PA, the characteristic peaks  $\text{NH}_2$  (3433, 3160, 810 ~ 616  $\text{cm}^{-1}$ ) and N-H (1570  $\text{cm}^{-1}$ ) of N-CNTs all disappeared at pH 2.0, indicating that BA and PA also could interact with these functional groups of N-CNTs by ordinary H-bonds. What is noteworthy is that, at pH 7.0, there was no new peak arose in the high frequency band after adsorption of BA, while a new peak (3660  $\text{cm}^{-1}$ ) did appear in the high-frequency band after adsorption of PA. This may be because the larger  $\Delta\text{pK}_a \approx 4.59$  (the difference is almost close to 5) between BA and N-CNTs leads to the formation of heteronuclear CAHB more likely to be an ordinary H-bond. Compared with BA, the smaller  $\Delta\text{pK}_a \approx 3.48$  between PA and N-CNTs makes the formation of heteronuclear CAHB much easier and stronger. For G-CNTs, due to the low oxygen content (0.22%, Table S1), there was no significant change in the characteristic peaks at pH 2.0 after adsorption of BA or PA, and there was also no blue shift H-bond that appeared at pH 7.0. These results are consistent with our above discussion in Sections 3.3 and 3.4, which further confirms that CAHB is an important mechanism for the adsorption of BA/PA on O-CNTs and N-CNTs. However, it is difficult to quantitatively analyze the bond strength and adsorption energy of homonuclear/heteronuclear CAHB on the molecular scale by using traditional spectral methods. DFT calculation can provide a deeper insight into the H-bond between CNTs and IOCs [29,52]. Therefore, DFT calculation is further employed to analyze the strength of homonuclear/heteronuclear CAHB formed between CNTs and BA/PA.

Figure 6. shows the optimized structures and calculation models of homonuclear/heteronuclear CAHB formed by O-CNTs and N-CNTs adsorbing BA or PA at pH 7.0. Table 1 displays the binding energy, bond length, and bond angle of homonuclear/heteronuclear CAHB. As we all know, the H-bond is more powerful when the bond length is shorter, and the bond angle is nearer to linearity (180°). For O-CNTs, homonuclear CAHB was formed with BA (CNTs-O $\cdots$ H $\cdots$ OOC-BA,  $-78.96 \text{ kJ}\cdot\text{mol}^{-1}$ ,  $178.814^\circ$ ,  $2.502 \text{ \AA}$ ; CNTs-COO $\cdots$ H $\cdots$ OOC-BA,  $-82.33 \text{ kJ}\cdot\text{mol}^{-1}$ ,  $178.994^\circ$ ,  $2.496 \text{ \AA}$ ) and PA (CNTs-O $\cdots$ H $\cdots$ OOC-PA,  $-81.49 \text{ kJ}\cdot\text{mol}^{-1}$ ,  $179.125^\circ$ ,  $2.518 \text{ \AA}$ ; CNTs-COO $\cdots$ H $\cdots$ OOC-PA,  $-88.12 \text{ kJ}\cdot\text{mol}^{-1}$ ,  $179.242^\circ$ ,  $2.507 \text{ \AA}$ ). For N-CNTs, heteronuclear CAHB was formed with BA (CNTs-NH $_2\cdots$ H $\cdots$ OOC-BA,  $-47.97 \text{ kJ}\cdot\text{mol}^{-1}$ ,  $177.592^\circ$ ,  $2.714 \text{ \AA}$ ) and PA (CNTs-NH $_2\cdots$ H $\cdots$ OOC-PA,  $-51.66 \text{ kJ}\cdot\text{mol}^{-1}$ ,  $177.157^\circ$ ,  $2.683 \text{ \AA}$ ). Obviously, compared with heteronuclear CAHB, homonuclear CAHB has higher adsorption energy, a shorter bond length, and a closer linear bond angle. It is worth noting that the heteronuclear CAHB between PA and N-CNTs is stronger than that between BA and N-CNTs. This is due to the smaller  $\Delta\text{pK}_a \approx 3.48$  between N-CNTs and PA relative to BA ( $\Delta\text{pK}_a \approx 4.59$ ), which is consistent with the above

description and conclusion. In conclusion, all the spectral evidence and DFT calculations indicate that homonuclear/heteronuclear CAHB plays an essential role in the adsorption of BA/PA by functionalized CNTs. Importantly, homonuclear CAHB is stronger than heteronuclear CAHB.

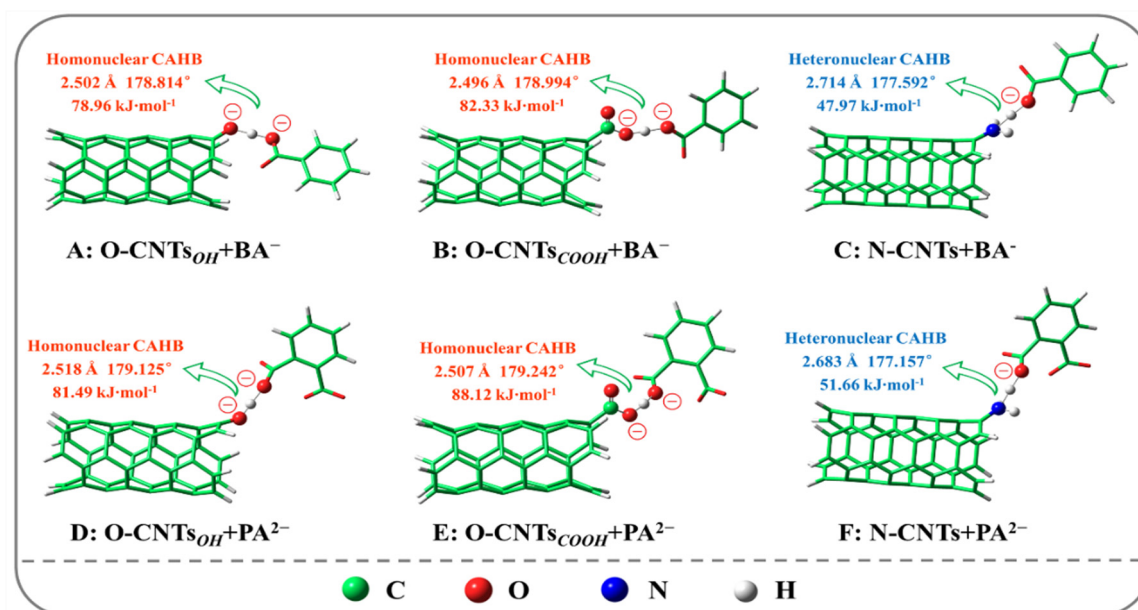


**Figure 6.** The Binding energy ( $E_{ads}$ , kJ·mol<sup>-1</sup>), bond length (Å) and bond angle (°) of charged assisted H-bonds (CAHBs) between CNTs and IOCs. The shorter bond length and the closer linear bond angle (180°) indicate the stronger H-bond, and the strength order of CAHBs is Homonuclear CAHB (A,B,D,E) > Heteronuclear CAHB (C,F).

**Table 1.** The binding energy ( $E_{ads}$ , kJ·mol<sup>-1</sup>), bond length (Å) and bond angle (°) of charged assisted H-bonds for BA and PA adsorption on O-CNTs and N-CNTs.

Adsorption configurations	$E_{ads}$ (kJ·mol <sup>-1</sup> )	Bond length (Å)	Bond angle (°)
O-CNTsOH ...BA <sup>-</sup>	−78.96	2.502	178.814
O-CNTsCOOH ...BA <sup>-</sup>	−82.33	2.496	178.994
N-CNTs...BA <sup>-</sup>	−47.97	2.714	177.592
O-CNTsOH ...PA <sup>2-</sup>	−81.49	2.518	179.125
O-CNTsCOOH ...PA <sup>2-</sup>	−88.12	2.507	179.242
N-CNTs...PA <sup>2-</sup>	−51.66	2.683	177.157

#### 4. Conclusions and Environmental Significance

In this study, the adsorption and desorption behaviors of BA and PA on three CNTs at different pHs were explored. The adsorption mechanism was discussed in detail by combining it with DFT simulation and FTIR characterization. The kinetics data implied that the adsorption of BA and PA on O-CNTs was mainly a chemical process at pH 7.0, especially and the negatively charged BA and PA could form strongly homonuclear CAHB with O-groups on the O-CNTs surface. For the adsorption isotherms, the Freundlich model was more appropriate than the Langmuir model, indicating BA and PA were more preferred to adsorb on the CNTs' surface. Under different pH conditions, the adsorption order of BA and PA on three CNTs was various. Especially at pH 4.0 and 7.0, the adsorption capacity of BA/PA on O-CNTs was clearly higher than that on N-CNTs, which can be attributed to CAHB formation, and the strength of homonuclear CAHB ( $\geq 78.96$  kJ·mol<sup>-1</sup>) was stronger than that of heteronuclear CAHB ( $\leq 51.66$  kJ·mol<sup>-1</sup>). In desorption assays under pH 7.0, the strong homonuclear CAHB formed between BA/PA and O-CNTs, leading to a clear desorption hysteresis phenomenon ( $HI \geq 3.51$ ). Compared with

the homonuclear CAHB, the relatively weaker heteronuclear CAHB between BA/PA and N-CNTs resulted in less significant desorption hysteresis ( $HI \geq 1.47$ ). Importantly, it was found that the contribution of homonuclear CAHB (BA: 54.17% and PA: 52.70%) was greater than that of heteronuclear CAHB (BA: 42.55% and PA: 45.79%) at pH 7.0. The above conclusions were further confirmed by FTIR characterization and DFT calculation, and the key evidence of CAHB in FTIR was found. Moreover, DFT calculation also provided pivotal information on the bond length and bond angle of homonuclear/heteronuclear CAHB at the molecular scale, which further revealed that homonuclear CAHB is stronger. Considering that different species' proportions of IOCs at different pHs would lead to different adsorption mechanisms, especially the role of CAHB should be carefully evaluated. In this study, DFT calculation and experimental tests were used to compare the strength of homonuclear/heteronuclear CAHB, which provides a new light for better comprehending the interaction between IOCs and carbonaceous materials. Moreover, the combination of DFT calculation, FTIR, and experiments would provide a new platform for studying the adsorption behavior between carbonaceous adsorbents and other organic and inorganic pollutants.

**Supplementary Materials:** The following supporting information can be downloaded at: <https://www.mdpi.com/article/10.3390/ijerph191912118/s1>: Table S1. Physicochemical properties of four different functionalized CNTs; Table S2. Selected physicochemical properties of BA and PA; Table S3. Kinetic fitting parameters of the pseudo-first order, pseudo-second order and intra-particle diffusion models for adsorption of BA and PA on O-CNTs; Table S4. Fitting parameters of Freundlich, Langmuir and Dubinin–Radushkevich models for BA and PA on CNTs at different pHs; Table S5. Release ratio ( $R_r$ , %) and hysteresis index of BA and PA from CNTs after three desorption steps at 298 K and various concentration (Low, Middle and High) of adsorbates. Low, Middle and High represent  $5 \text{ mg} \cdot \text{L}^{-1}$ ,  $80 \text{ mg} \cdot \text{L}^{-1}$  and  $160 \text{ mg} \cdot \text{L}^{-1}$  of BA/PA; Figure S1. Adsorption equilibrium time of BA and PA onto O-CNTs at different pHs. The initial concentration was  $50 \text{ mg} \cdot \text{L}^{-1}$  for adsorbates. There is no significant difference in  $Q_e$  after 48 h. Thus, we consider that 48 h is long enough to achieve adsorption equilibrium; Figure S2. Optimized structures of CNTs (A: O-CNTs-OH, B: O-CNTs-COOH C: N-CNTs), BA (D) and PA (E). Figure S3. TEM and SEM images of O-CNTs (A and D), N-CNTs (B and E) and G-CNTs (C and F), respectively; Figure S4. Pore size distributions of O-CNTs, N-CNTs and G-CNTs, respectively. Figure S5. Peak fitting of O1s for O-CNTs; Figure S6. FTIR spectra of O-CNTs, N-CNTs and G-CNTs at room temperature at the range of  $400\text{--}4000 \text{ cm}^{-1}$ ; Figure S7. The speciation distribution diagram of BA and PA in water at different pHs; Figure S8. Adsorption and desorption of PA on O-CNTs, N-CNTs and G-CNTs at pH 2.0 (A, B and C) and pH 7.0 (D, E and F), respectively. And the comparison of the hysteresis index of PA (low, middle and high represent 5, 80 and  $160 \text{ mg} \cdot \text{L}^{-1}$  of PA, respectively) adsorption on three types of CNTs (G, H and I) at pH 2.0 and pH 7.0. At pH 2.0, there is no obvious desorption hysteresis of PA on three CNTs, but the obvious desorption hysteresis of PA on O-CNTs and N-CNTs occurred at pH 7.0. The hysteresis index of PA on O-CNTs ( $\geq 3.51$ ) and N-CNTs ( $\geq 2.60$ ) is higher than that of BA on G-CNTs ( $\leq 0.94$ ) at pH 7.0.

**Author Contributions:** Conceptualization, X.L. and Q.C.; methodology, J.Z.; software, Y.J.; Y.L.; N.L. and Z.X.; formal analysis, Y.J.; Y.L. and N.L.; investigation, J.Z. and C.D.; data curation, J.Z.; Y.J.; Y.W. and N.Z.; writing—original draft preparation, X.L.; writing—review and editing, X.L., J.Z. and Q.C.; supervision, X.L.; project administration, X.L.; funding acquisition, X.L.; Y.L. and Q.C. All authors have read and agreed to the published version of the manuscript.

**Funding:** This work was supported by the National Natural Science Foundation of China (42177202, 41703093, 41907148), Key R&D project of Shaanxi Province (2022NY-054), the Fundamental Research Funds for the Central University (GK202103138, 2021CSLY015, GK202103128).

**Institutional Review Board Statement:** Not applicable.

**Informed Consent Statement:** Not applicable.

**Data Availability Statement:** Further information can be obtained from the corresponding author.

**Acknowledgments:** We very much appreciate Yuanyuan Wang, Jia Chen, and Yanfei Tian for their help in the experiments.



**Conflicts of Interest:** The authors declare no conflicts of interest in this work.

## References

- Kah, M.; Sigmund, G.; Xiao, F.; Hofmann, T. Sorption of ionizable and ionic organic compounds to biochar, activated carbon and other carbonaceous materials. *Water Res.* **2017**, *124*, 673–692. <https://doi.org/10.1016/j.watres.2017.07.070>.
- Sigmund, G.; Arp, H.; Aumeier, B.; Bucheli, T.; Chefetz, B.; Chen, W.; Droge, S.; Endo, S.; Escher, B.; Hale, S.; Hofmann, T.; Pignatello, J.; Reemtsma, T.; Schmidt, T.; Schönsee, C.; Scheringer, M. Sorption and Mobility of Charged Organic Compounds: How to Confront and Overcome Limitations in Their Assessment. *Environ. Sci. Technol.* **2022**, *56*, 4702–4710. <https://doi.org/10.1021/acs.est.2c00570>
- Manjarres-Lopez, D.P.; Andrades, M.S.; Sanchez-Gonzalez, S.; Rodriguez-Cruz, M.S.; Sanchez-Martin, M.J.; Herrero-Hernandez, E. Assessment of pesticide residues in waters and soils of a vineyard region and its temporal evolution. *Environ. Pollut.* **2021**, *284*, 117463. <https://doi.org/10.1016/j.envpol.2021.117463>.
- Kurwadkar, S.; Dane, J.; Kanel, S.R.; Nadagouda, M.N.; Cawdrey, R.W.; Ambade, B.; Struckhoff, G.C.; Wilkin, R. Per- and polyfluoroalkyl substances in water and wastewater: A critical review of their global occurrence and distribution. *Sci. Total Environ.* **2022**, *809*, 151003. <https://doi.org/10.1016/j.scitotenv.2021.151003>.
- Ma, L.; Liu, Y.; Yang, Q.; Jiang, L.; Li, G. Occurrence and distribution of Pharmaceuticals and Personal Care Products (PPCPs) in wastewater related riverbank groundwater. *Sci. Total Environ.* **2022**, *821*, 153372. <https://doi.org/10.1016/j.scitotenv.2022.153372>.
- Vitale, C.M.; Di Guardo, A. A review of the predictive models estimating association of neutral and ionizable organic chemicals with dissolved organic carbon. *Sci. Total Environ.* **2019**, *666*, 1022–1032. <https://doi.org/10.1016/j.scitotenv.2019.02.340>.
- Zhou, J.; Saeidi, N.; Wick, L.Y.; Kopinke, F.D.; Georgi, A. Adsorption of polar and ionic organic compounds on activated carbon: Surface chemistry matters. *Sci. Total Environ.* **2021**, *794*, 148508. <https://doi.org/10.1016/j.scitotenv.2021.148508>.
- Karlsson, M.V.; Carter, L.J.; Agatz, A.; Boxall, A.B.A. Novel Approach for Characterizing pH-Dependent Uptake of Ionizable Chemicals in Aquatic Organisms. *Environ. Sci. Technol.* **2017**, *51*, 6965–6971. <https://doi.org/10.1021/acs.est.7b01265>.
- Bueno, M.J.M.; Valverde, M.G.; Gomez-Ramos, M.M.; Andujar, J.A.S.; Barcelo, D.; Fernandez-Alba, A.R. Fate, modeling, and human health risk of organic contaminants present in tomato plants irrigated with reclaimed water under real-world field conditions. *Sci. Total Environ.* **2022**, *806*, 150909. <https://doi.org/10.1016/j.scitotenv.2021.150909>.
- Tang, H.; Zhao, Y.; Yang, X.; Liu, D.; Shan, S.; Cui, F.; Xing, B. Understanding the pH-dependent adsorption of ionizable compounds on graphene oxide using molecular dynamics simulations. *Environ. Sci. Nano* **2017**, *4*, 1935–1943. <https://doi.org/10.1039/c7en00585g>.
- Li, H.; Cao, Y.; Zhang, D.; Pan, B. pH-dependent KOW provides new insights in understanding the adsorption mechanism of ionizable organic chemicals on carbonaceous materials. *Sci. Total Environ.* **2018**, *618*, 269–275. <https://doi.org/10.1016/j.scitotenv.2017.11.065>.
- Chen, J.; Zhang, D.; Zhang, H.; Ghosh, S.; Pan, B. Fast and slow adsorption of carbamazepine on biochar as affected by carbon structure and mineral composition. *Sci. Total Environ.* **2017**, *579*, 598–605. <https://doi.org/10.1016/j.scitotenv.2016.11.052>.
- Sigmund, G.; Gharasoo, M.; Huffer, T.; Hofmann, T. Deep Learning Neural Network Approach for Predicting the Sorption of Ionizable and Polar Organic Pollutants to a Wide Range of Carbonaceous Materials. *Environ. Sci. Technol.* **2020**, *54*, 4583–4591. <https://doi.org/10.1021/acs.est.9b06287>.
- Chen, Z.; Ji, W. Sorption of ionizable organic chemicals to carbonaceous adsorbents: Solution pH change and contributions of different species. *Sci. Total Environ.* **2019**, *647*, 1069–1079. <https://doi.org/10.1016/j.scitotenv.2018.08.033>.
- Yang, Y.; Zheng, L.; Zhang, T.; Yu, H.; Zhan, Y.; Yang, Y.; Zeng, H.; Chen, S.; Peng, D. Adsorption behavior and mechanism of sulfonamides on phosphonic chelating cellulose under different pH effects. *Bioresour. Technol.* **2019**, *288*, 121510. <https://doi.org/10.1016/j.biortech.2019.121510>.
- Liang, D.; Yu, F.; Zhu, K.; Zhang, Z.; Tang, J.; Xie, Q.; Liu, J.; Xie, F. Quaternary ammonium salts targeted regulate the surface charge distribution of activated carbon: A study of their binding modes and modification effects. *Environmental Research*, **2022**, *214*: 11410.
- Roman, M.; Gutierrez, L.; Van Dijk, L.H.; Vanoppen, M.; Post, J.W.; Wols, B.A.; Cornelissen, E.R.; Verliefde, A.R.D. Effect of pH on the transport and adsorption of organic micropollutants in ion-exchange membranes in electrodialysis-based desalination. *Sep. Purif. Technol.* **2020**, *252*, 117487. <https://doi.org/10.1016/j.seppur.2020.117487>.
- Zhang, J.; Zhai, J.; Zheng, H.; Li, X.; Wang, Y.; Li, X.; Xing, B. Adsorption, desorption and coadsorption behaviors of sulfamerazine, Pb(II) and benzoic acid on carbon nanotubes and nano-silica. *Sci. Total Environ.* **2020**, *738*, 139685. <https://doi.org/10.1016/j.scitotenv.2020.139685>.
- Luo, Z.; Yao, B.; Yang, X.; Wang, L.; Xu, Z.; Yan, X.; Tian, L.; Zhou, H.; Zhou, Y. Novel insights into the adsorption of organic contaminants by biochar: A review. *Chemosphere* **2022**, *287*, 132113. <https://doi.org/10.1016/j.chemosphere.2021.132113>.
- Li, M.; Liu, Y.; Yang, C.; Liu, S.; Tan, X.; He, Y.; Liu, N.; Zhou, L.; Cai, X.; Wen, J. Effects of heteroaggregation with metal oxides and clays on tetracycline adsorption by graphene oxide. *Sci. Total Environ.* **2020**, *719*, 137283. <https://doi.org/10.1016/j.scitotenv.2020.137283>.

21. Pan, B.; Xing, B. Adsorption Mechanisms of Organic Chemicals on Carbon Nanotubes. *Environ. Sci. Technol.* **2008**, *42*, 9005–9013. <https://doi.org/10.1021/es801777n>
22. Lin, D.; Li, T.; Yang, K.; Wu, F. The relationship between humic acid (HA) adsorption on and stabilizing multiwalled carbon nanotubes (MWNTs) in water: Effects of HA, MWNT and solution properties. *J. Hazard. Mater.* **2012**, *241–242*, 404–410. <https://doi.org/10.1016/j.jhazmat.2012.09.060>
23. Wang, H.; Shan, L.; Lv, Q.; Cai, S.; Quan, G.; Yan, J. Production of hierarchically porous carbon from natural biomass waste for efficient organic contaminants adsorption. *J. Clean. Prod.* **2020**, *263*, 121352. <https://doi.org/10.1016/j.jclepro.2020.121352>
24. Ni, J.; Pignatello, J.J.; Xing, B. Adsorption of aromatic carboxylate ions to black carbon (biochar) is accompanied by proton exchange with water. *Environ. Sci. Technol.* **2011**, *45*, 9240–9248. <https://doi.org/10.1021/es201859j>
25. Li, X.; Gamiz, B.; Wang, Y.; Pignatello, J.J.; Xing, B. Competitive sorption used to probe strong hydrogen bonding sites for weak organic acids on carbon nanotubes. *Environ. Sci. Technol.* **2015**, *49*, 1409–1417. <https://doi.org/10.1021/es504019u>
26. Li, X.; Pignatello, J.J.; Wang, Y.; Xing, B. New insight into adsorption mechanism of ionizable compounds on carbon nanotubes. *Environ. Sci. Technol.* **2013**, *47*, 8334–8341. <https://doi.org/10.1021/es4011042>
27. Ling, C.; Li, X.; Zhang, Z.; Liu, F.; Deng, Y.; Zhang, X.; Li, A.; He, L.; Xing, B. High Adsorption of Sulfamethoxazole by an Amine-Modified Polystyrene-Divinylbenzene Resin and Its Mechanistic Insight. *Environ. Sci. Technol.* **2016**, *50*, 10015–10023. <https://doi.org/10.1021/acs.est.6b02846>
28. Zhao, J.; Chu, G.; Pan, B.; Zhou, Y.; Wu, M.; Liu, Y.; Duan, W.; Lang, D.; Zhao, Q.; Xing, B. Homo-Conjugation of Low Molecular Weight Organic Acids Competes with Their Complexation with Cu(II). *Environ. Sci. Technol.* **2018**, *52*, 5173–5181. <https://doi.org/10.1021/acs.est.7b05965>
29. Wang, P.; Zhang, D.; Tang, H.; Li, H.; Pan, B. New insights on the understanding of the high adsorption of bisphenol compounds on reduced graphene oxide at high pH values via charge assisted hydrogen bond. *J. Hazard. Mater.* **2019**, *371*, 513–520. <https://doi.org/10.1016/j.jhazmat.2019.03.012>
30. Gilli, G.; Gilli, P. Towards an unified hydrogen-bond theory. *J. Mol. Struct.* **2000**, *552*, 1–15. [https://doi.org/10.1016/S0022-2860\(00\)00454-3](https://doi.org/10.1016/S0022-2860(00)00454-3)
31. Gilli, P.; Pretto, L.; Bertolasi, V.; Gilli, G. Predicting Hydrogen-Bond Strengths from Acid–Base Molecular Properties. The pKa Slide Rule: Toward the Solution of a Long-Lasting Problem. *Acc. Chem. Res.* **2009**, *42*, 33–44. <https://doi.org/10.1021/ar800001k>
32. Xiao, F.; Pignatello, J.J. Effects of Post-Pyrolysis Air Oxidation of Biomass Chars on Adsorption of Neutral and Ionizable Compounds. *Environ. Sci. Technol.* **2016**, *50*, 6276–6283. <https://doi.org/10.1021/acs.est.6b00362>
33. Del Olmo, A.; Calzada, J.; Nunez, M. Benzoic acid and its derivatives as naturally occurring compounds in foods and as additives: Uses, exposure, and controversy. *Crit. Rev. Food Sci. Nutr.* **2017**, *57*, 3084–3103. <https://doi.org/10.1080/10408398.2015.1087964>
34. Karunanayake, A.G.; Todd, O.A.; Crowley, M.L.; Ricchetti, L.B.; Pittman, C.U.; Anderson, R.; Mlsna, T.E. Rapid removal of salicylic acid, 4-nitroaniline, benzoic acid and phthalic acid from wastewater using magnetized fast pyrolysis biochar from waste Douglas fir. *Chem. Eng. J.* **2017**, *319*, 75–88. <https://doi.org/10.1016/j.cej.2017.02.116>
35. Dai, J.; Xiao, X.; Duan, S.; Liu, J.; He, J.; Lei, J.; Wang, L. Synthesis of novel microporous nanocomposites of ZIF-8 on multiwalled carbon nanotubes for adsorptive removing benzoic acid from water. *Chem. Eng. J.* **2018**, *331*, 64–74. <https://doi.org/10.1016/j.cej.2017.08.090>
36. Hannon, P.R.; Flaws, J.A. The effects of phthalates on the ovary. *Front. Endocrinol.* **2015**, *6*, 8. <https://doi.org/10.3389/fendo.2015.00008>
37. Shuai, W.; Gu, C.; Fang, G.; Zhou, D.; Gao, J. Effects of iron (hydr)oxides on the degradation of diethyl phthalate ester in heterogeneous (photo)-Fenton reactions. *J. Environ. Sci.* **2019**, *80*, 5–13. <https://doi.org/10.1016/j.jes.2018.06.015>
38. Shahid, M.K.; Kashif, A.; Fuwad, A.; Choi, Y. Current advances in treatment technologies for removal of emerging contaminants from water—A critical review. *Coord. Chem. Rev.* **2021**, *442*, 213993. <https://doi.org/10.1016/j.ccr.2021.213993>
39. Khan, N.A.; Jung, B.K.; Hasan, Z.; Jhung, S.H. Adsorption and removal of phthalic acid and diethyl phthalate from water with zeolitic imidazolate and metal-organic frameworks. *J. Hazard. Mater.* **2015**, *282*, 194–200. <https://doi.org/10.1016/j.jhazmat.2014.03.047>
40. Tielens, F.; Folliet, N.; Bondaz, L.; Etemovic, S.; Babonneau, F.; Gervais, C.; Azais, T. Molecular Picture of the Adsorption of Ibuprofen and Benzoic Acid on Hydrated Amorphous Silica through DFT-D Calculations Combined with Solid-State NMR Experiments. *J. Phys. Chem. C* **2017**, *121*, 17339–17347. <https://doi.org/10.1021/acs.jpcc.7b05045>
41. Xu, Y.; Jang, J.; Gye, M.C. The *Xenopus laevis* teratogenesis assay for developmental toxicity of phthalate plasticizers and alternatives. *Environ. Pollut.* **2022**, *300*, 118985. <https://doi.org/10.1016/j.envpol.2022.118985>
42. Vuković, G.D.; Marinković, A.D.; Škapin, S.D.; Ristić, M.D.; Aleksić, R.; Perić-Grujić, A.A.; Uskoković, P.S. Removal of lead from water by amino modified multi-walled carbon nanotubes. *Chem. Eng. J.* **2011**, *173*, 855–865. <https://doi.org/10.1016/j.cej.2011.08.036>
43. Li, J.; Chen, S.; Sheng, G.; Hu, J.; Tan, X.; Wang, X. Effect of surfactants on Pb(II) adsorption from aqueous solutions using oxidized multiwall carbon nanotubes. *Chem. Eng. J.* **2011**, *166*, 551–558. <https://doi.org/10.1016/j.cej.2010.11.018>
44. Alqadami, A.A.; Naushad, M.; ZA, A.L.; Alsuhbani, M.; Algamdi, M. Excellent adsorptive performance of a new nanocomposite for removal of toxic Pb(II) from aqueous environment: Adsorption mechanism and modeling analysis. *J. Hazard. Mater.* **2020**, *389*, 121896. <https://doi.org/10.1016/j.jhazmat.2019.121896>

45. Sun, T.; Fan, H.; Zhuo, Q.; Liu, X.; Wu, Z. Covalent incorporation of aminated carbon nanotubes into epoxy resin network. *High Perform. Polym.* **2014**, *26*, 892–899. <https://doi.org/10.1177/0954008314533810>.
46. Ramanathan, T.; Fisher, F.T.; Ruoff, R.S.; Brinson, L.C. Amino-Functionalized Carbon Nanotubes for Binding to Polymers and Biological Systems. *Chem. Mater.* **2005**, *17*, 1290–1295. <https://doi.org/10.1021/cm048357f>.
47. Ehsan, S.P.; Hossein, A.; Mohamad, E.; Hooman, F.; Seyed, J.H.; Alireza, S. Batch adsorptive removal of benzoic acid from aqueous solution onto modified natural vermiculite: Kinetic, isotherm and thermodynamic studies. *J. Ind. Eng. Chem.* **2015**, *31*, 1–17. <https://doi.org/10.1016/j.jiec.2015.06.024>.
48. Caliskan, N.; Kul, A.R.; Alkan, S.; Sogut, E.G.; Alacabey, I. Adsorption of Zinc(II) on diatomite and manganese-oxide-modified diatomite: A kinetic and equilibrium study. *J. Hazard. Mater.* **2011**, *193*, 27–36. <https://doi.org/10.1016/j.jhazmat.2011.06.058>.
49. Liu, J.; Ma, Y.; Zhu, D.; Xia, T.; Qi, Y.; Yao, Y.; Guo, X.; Ji, R.; Chen, W. Polystyrene Nanoplastics-Enhanced Contaminant Transport: Role of Irreversible Adsorption in Glassy Polymeric Domain. *Environ. Sci. Technol.* **2018**, *52*, 2677–2685. <https://doi.org/10.1021/acs.est.7b05211>.
50. Barnes, A.J. Blue-shifting hydrogen bonds—are they improper or proper? *J. Mol. Struct.* **2004**, *704*, 3–9. <https://doi.org/10.1016/j.molstruc.2004.02.040>.
51. Li, X.; Liu, L.; Schlegel, H.B. On the Physical Origin of Blue-Shifted Hydrogen Bonds. *J. Am. Chem. Soc.* **2002**, *124*, 9639–9647. <https://doi.org/10.1021/ja020213j>.
52. Tang, H.; Zhao, Y.; Shan, S.; Yang, X.; Liu, D.; Cui, F.; Xing, B. Wrinkle- and Edge-Adsorption of Aromatic Compounds on Graphene Oxide as Revealed by Atomic Force Microscopy, Molecular Dynamics Simulation, and Density Functional Theory. *Environ. Sci. Technol.* **2018**, *52*, 7689–7697. <https://doi.org/10.1021/acs.est.8b00585>.